Achieving Strong Coherency for Composite Electrode via One Pot Method with Enhanced Electrochemical Performance in Reversible Solid Oxide Cells

Yunfeng Tian [a], Wenjie Wang [b], Yun Liu [b], Aaron Naden [c], Min Xu [c],

Shitao Wu [c], Bo Chi [b, d]*, Jian Pu [b, d], John T.S. Irvine [c]

[a] School of Materials Science and Physics, China University of Mining and Technology, Xuzhou, 221116, China

[b] Center for Fuel Cell Innovation, School of Materials Science and Engineering, Huazhong University of Science and Technology, Wuhan 430074, China

[c] School of Chemistry, University of St Andrews, St Andrews, Fife, KY16 9ST Scotland, UK

[d] Key Laboratory of Material Chemistry for Energy Conversion and Storage of Ministry of Education, Huazhong University of Science and Technology, Wuhan 430074, China

*Corresponding author.

E-mail: chibo@hust.edu.cn (Bo. Chi)

ABSTRACT: The oxygen electrode with fast oxygen reduction reaction (ORR), oxygen evolution reaction (OER) and sufficient durability plays a pivotal role in reversible solid oxide cells (RSOCs). Here we demonstrate a novel $NdBa_{0.5}Ca_{0.5}Co_{1.5}Fe_{0.5}O_{5+\delta}@Gd_{0.1}Ce_{0.9}O_{2-\delta}$ (NBCCF@GDC) composite oxygen electrode via a one-pot method for exhibiting strong coherency, which resulting in boosting electrochemical performance of RSOCs. The NBCCF@GDC electrode yields a very low polarization resistance ($0.106 \ \Omega \ cm^2$ at 800 °C), high electrolysis current density ($1.45 \ A \ cm^{-2}$ with 70 vol% absolute humidity at 1.3 V), high power density ($\sim 1.3 \ W \ cm^{-2}$ at 800 °C) and shows excellent reversibility and stability. Notably, strong coherency in these NBCCF@GDC composite materials was successfully revealed by HT-XRD, XPS, STEM and EELS. The phase contiguity and interfacial coherence between NBCCF and GDC increase the Co oxidation state and the number of active sites, which enhanced the electrocatalytic activity for perovskites. Overall, this work demonstrates a highly desirable strategy for the production of functionalized electrodes for next generation reversible solid oxide cells.

KEYWORDS: One-pot method; Oxygen electrode; NBCCF@GDC composite; Reversible solid oxide cells; Strong coherency

1. Introduction

Increasing energy demand and the environmental impact of fossil fuels pose great challenges to modern society [1]. Therefore, numerous new energy technologies have been developed to address these problems [2-5]. Among them, reversible solid oxide cells (RSOCs) have been favored due to their high efficiency and their use of more environmentally-friendly fuels/by-products [6, 7]. They can convert the chemical energy of fuel (H_2, CO, CH_4, etc) into clean electric energy in the fuel cell mode (SOFC), or use the intermittent clean energy (wind, solar, tidal energy, etc.) to electrolyze H_2O or CO_2 for energy storage in the electrolysis mode (SOEC) [8, 9].

In the sandwich structure of RSOCs (hydrogen electrode, electrolyte and oxygen electrode), the oxygen electrode plays a pivotal role in the oxygen reduction reaction (ORR) and oxygen evolution reaction (OER) in fuel cell and electrolysis mode, respectively. Their slowness acts as a rate-limiting step. Also, they often use oxides of Ir or Pt which are expensive materials. Therefore, a number of studies have focused on the development of high performance oxygen electrode. Double perovskite (DP) oxides with formula of $AA'BB'O_6$ (where A is rare-earth metal, A' is an alkali or alkaline earth metal and B, B' is a transition metal) have superior mixed ionic conductivities and oxygen surface exchange coefficient. This type of perovskite material has aroused widespread research interest. SOFCs based on these cathode materials with ORR activity have achieved good electrochemical performance: for example, $PrBa_{0.5}Sr_{0.5}Co_{1.5}Fe_{0.5}O_{5+\delta}$ (0.986 W cm^{-2} at 800 °C) [10], $SmBa_{0.5}Sr_{0.5}Co_{1.5}Fe_{0.5}O_{5+\delta}$ (1.56 W cm^{-2} at 600 °C) [11], $NdBa_{0.5}Sr_{0.5}Co_2O_{5+\delta}$ (1.086 W cm^{-2} at 600 °C) [12]. In addition, a number of studies have demonstrated that Ca-doping in double perovskite oxides can reduce thermal expansion coefficient (TEC), facilitate electrical conductivity and provide higher oxygen vacancy concentrations [13-16]. In particular, Hua et al. have reported on $NdBa_{0.75}Ca_{0.25}Co_{1.5}Fe_{0.5}O_{5+\delta}$ with excellent ORR catalytic performance at both room and elevated temperatures [17]. However, relatively little investigation has been reported on this

system's OER performance at high temperature so far.

Another major stumbling blocks for the commercialization of new electrode materials are reliable material synthesis and their incorporation via appropriate cell manufacturing methods. Physically mixing the electrode with electrolyte ((La, Sr)MnO_3-$Y_{0.08}Zr_{0.92}O_2$, (La, Sr)(Co, Fe)O_3-$Gd_{0.1}Ce_{0.9}O_2$, etc.) as composite oxygen electrodes can increase the number of triple phase boundaries (TPB) and hence improve the electrocatalytic performance [18, 19]. Other approaches are the production of nanostructured composite electrodes by impregnation of the perovskite into the electrolyte skeleton [20, 21] and exsolution of nanoparticles from the perovskite matrix for high performance oxygen electrodes [22-24]. However, the inhomogeneity of physical mixing and particle coarsening or agglomeration are the main challenges [25-27]. Furthermore, the complex synthesis procedure, specialized facilities and extreme experimental conditions are often required for preparing these materials. These factors can make cost-effective and large-scale production extremely challenging. Therefore, an economical and reliable electrode preparation method is urgently needed to develop.

Here we demonstrate a rapid, low-cost and low-energy one-pot technique to synthesize $NdBa_{0.5}Ca_{0.5}Co_{1.5}Fe_{0.5}O_{5+\delta}@Gd_{0.1}Ce_{0.9}O_{2-\delta}$ composite oxygen electrodes, which exhibiting strong coherency outperforms physical contact between NBCCF and GDC. Notably, strong coherency in these NBCCF@GDC composite materials was successfully revealed by HT-XRD, XPS, STEM and EELS. RSOCs based on this novel composite oxygen electrode can achieve excellent electrocatalytic performance and stability both in SOFC and SOEC modes. Specifically, this technique can prepare electrodes with lower polarization resistance, higher power density and higher electrolysis current density compared with those prepared by traditional physical mixing method at reduced cost. These results demonstrate that this novel technique provides exciting new opportunities for performance enhancement of oxygen electrode for RSOCs.

2. Experimental

2.1 Sample and cell preparation

$NdBa_{0.5}Ca_{0.5}Co_{1.5}Fe_{0.5}O_{5+\delta}@Gd_{0.1}Ce_{0.9}O_{2-\delta}$ (NBCCF@GDC) powders with the weight ratio of 60:40 were prepared by one-pot method as shown in Fig. 1, using $Nd(NO_3)_3$ $6H_2O$, $Ba(NO_3)_2$, $Ca(NO_3)_2$ $4H_2O$, $Co(NO3)_2$ $6H_2O$, $Fe(NO3)_3$ $9H_2O$, $Gd(NO_3)_3$ $6H_2O$, $Ce(NO_3)_3$ $6H_2O$, citric acid (CA), ethylenediaminetetraacetic acid (EDTA) and ammonia solution as precursors. All nitrates were purchased from Sigma-Aldrich. Firstly, all stoichiometric nitrates were dissolved in deionized water and then added to EDTA and CA with the metal ions/EDTA/CA in a molar ratio of 1:1:1.5. The pH value of the aqueous solution was adjusted to 7 by ammonia solution and then stirred on a hot plate until the gel was formed. The gel was heat-treated at 300 °C in an oven for 10 h before calcination at 1000 °C in air for 2 h to obtain the final NBCCF@GDC sample. Pure NBCCF and GDC powders were also synthesized separately by the sol-gel method [10, 28].
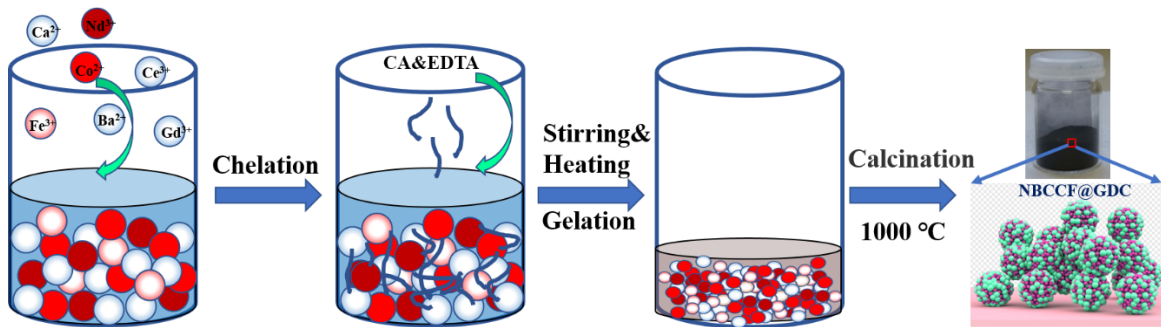

Fig. 1 Schematic of one-pot synthesis of NBCCF@GDC.

Symmetrical cell configurations of NBCCF@GDC/GDC/YSZ/GDC/NBCCF@GDC were prepared to evaluate the polarization resistance of NBCCF@GDC. For full cell performance measurements, the cell configuration Ni-YSZ/YSZ/GDC/NBCCF@GDC was prepared, and hydrogen electrode-supported (Ni-YSZ), Ni-YSZ functional layer, YSZ electrolyte were fabricated by tape-casting and screen-printing method. The detailed preparation steps can be found in our previous works [29, 30]. The GDC buffer layer was used to prevent the possible chemical reaction

between the oxygen electrode and electrolyte. The NBCCF@GDC powders were mixed with a binder (4% ethylcellulose dissolved in terpineol) in a mass ratio of 60:40 to form a paste. Then NBCCF@GDC paste was screen-printed on the GDC surface and fired at 1000 °C in air for 2 h to obtain the final cell. The symmetrical cell and full cell with physical mixing NBCCF-GDC composite electrode (60 wt%:40 wt%) were also prepared for comparison. All cells have active areas of 0.5 cm^2 and Pt slurry was used as the current collector.

2.2 Characterization and measurements

The phase purity and crystal structure of NBCCF@GDC, NBCCF and GDC were characterized by X-ray diffraction (XRD, Shimadzu XRD-7000S). In-situ high temperature XRD was used to confirm the formation of NBCCF@GDC from room temperature to 850 °C using a PANalytical Empyrean X-ray diffractometer (Mo Ka1,2). Morphology of physical mixing NBCCF-GDC powders, NBCCF@GDC powders and Ni-YSZ/YSZ/GDC/NBCCF@GDC cell were characterized using field emission scanning electron microscopy (FESEM, Zeiss Neon 40EsB and Supra-55 Sapphire) combined with energy dispersive spectroscopy (EDS). Transmission electron microscopy (TEM), EDS analysis and electron energy loss spectroscopy (EELS) analysis were performed on a FEI Titan Themis instrument. Thin lamella was prepared for TEM by focused ion beam (FIB) using a FEI Scios scanning electron microscope (SEM). TGA (STA449F5, NETZSCH) was used to characterize the thermophysical property of NBCCF@GDC and NBCCF-GDC from room temperature to 1000 °C with a heating rate of 10 °C min^{-1} under air. The surface areas were determined by the Brunauer-Emmet-Teller (BET) method using Micromeritics ASAP2020. The thermal expansion coefficient (TEC) was measured by Netzsch Dilatometer DIL402C and the conductivity tests were conducted by a four-probe method using dense bar (20 mm×5 mm×1.5 mm) calcined at 1250 °C for 5 h. The surface element distribution of the samples was evaluated by X-ray photoelectron spectroscopy (XPS, VG Multilab 2000) using Al Kα

radiation (hv = 1486.6 eV) and the spectra were calibrated by the C1s peak 284.8 eV. Fourier-transform infra-red (FT-IR) spectra were recorded at room temperature on a Shimadzu IRAffinity 1S IR Spectrometer.

The symmetrical cell was tested in air at different temperatures. For the full cell test, it was sealed on an Al_2O_3 tube using ceramic adhesive (552-VFG, Aremco). In SOFC mode, humidified hydrogen and air were fed into the hydrogen and the oxygen electrodes, respectively, at flow rates of 100 ml min^{-1}. In SOEC mode, the saturated steam concentration and the ratio of H_2O-CO_2 were controlled by a thermostatic water bath. The electrochemical performance of SOCs was measured by an electrochemical workstation (Zennium IM6 station), including the current density-voltage curves, electrochemical impedance spectra (the frequency range of 0.1-100 kHz with an amplitude of 10 mV), the reversibility and stability of SOCs in SOFC and SOEC mode. Electrochemical impedance spectra were analyzed by distribution of relaxation time (DRT) [31, 32]. The microstructure and element distribution of full cell after test were observed by environmental scanning electron microscope (ESEM, Quanta 200).

3. Results and discussion

3.1. Physicochemical properties

The crystal structure of the as-prepared NBCCF@GDC composites was investigated by XRD. Fig. 2(a) shows the XRD patterns of the NBCCF, GDC and NBCCF@GDC powders. It can be observed that the fluorite structure is assigned for GDC while NBCCF presents a double perovskite phase without any detectable impurity peaks. For the NBCCF@GDC powders, only the expected diffraction peaks from NBCCF and GDC are observed, indicating that NBCCF and GDC have good chemical compatibility. This therefore confirms that the NBCCF@GDC fired at 1000 °C can form two individual phases rather than a unique phase (Fig. 2(b)), suggesting that the one-pot method is an effective and facile way to prepare such NBCCF@GDC composite. The TG curves

of NBCCF@GDC and NBCCF-GDC under air are recorded in Fig. 2(c). The weight change at the higher temperature range is attributed to the formation of oxygen vacancies. NBCCF@GDC has the large weight loss compared with NBCCF-GDC indicating that it has more oxygen vacancies. Oxygen vacancies are generally regarded as the reactive sites and contribute to the enhancement of ORR and OER performance [33]. The BET specific surface area of NBCCF@GDC is 16.10 m^2 g^{-1} as shown in Fig. 2(d), which is 5 times higher than that of NBCCF-GDC. This is because NBCCF@GDC powders synthesized by the one-pot method are fine and uniform. Crucially, NBCCF@GDC shows better conductivity comparable to that of NBCCF-GDC in air at all test temperatures, as shown in Fig. 2(e). This phenomenon is likely due to the presence of interconnected networks of electronic conductance in NBCCF@GDC arising from the uniform distribution of NBCCF. In addition, NBCCF@GDC shows a lower TEC (17.6*10^{-6} K^{-1}) than NBCCF-GDC (21.3*10^{-6} K^{-1}) as shown in Fig. 2(f), making it more compatible with GDC buffer layer [34]. The reduced TEC value may originate from the suppressed chemical expansion of Co ions, since the high TEC of Co-based perovskite is mainly due to the transition of the spin state of Co ions and the reduction of the valence state of Co ions [35, 36].
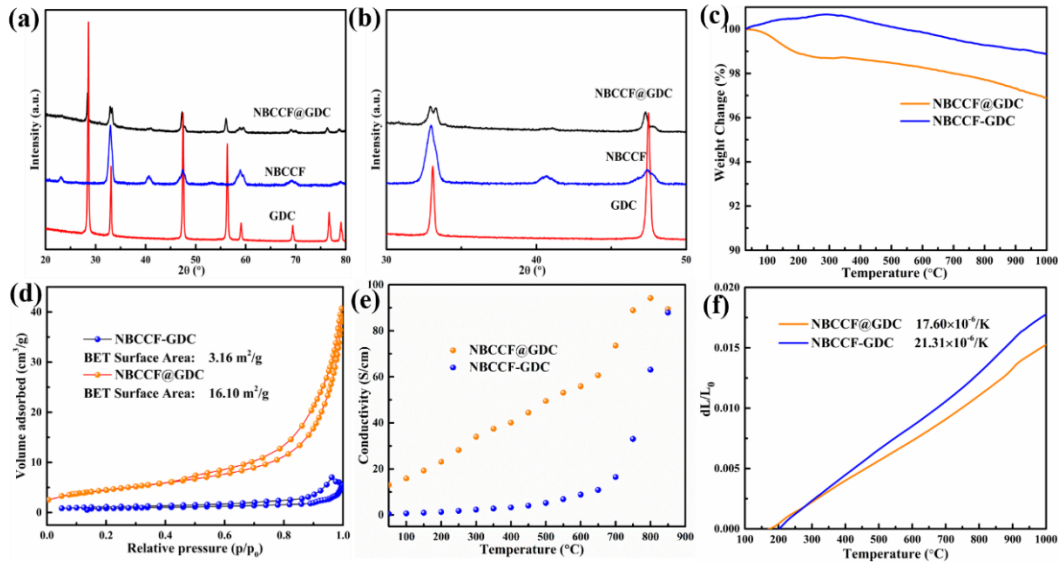
Fig. 2 XRD patterns of NBCCF, GDC and NBCCF@GDC (a and b); TG curves in air (c); BET curves (d); TEC curves (e) and electrical conductivities (f) of NBCCF@GDC and NBCCF-GDC.

3.2. Morphology

Fig. 3(a) displays the cross-sectional morphology of the single cell, including porous Ni-YSZ supporting layer and fuel electrode, dense electrolyte YSZ with GDC buffer layer, and porous NBCCF@GDC oxygen electrode. Detailed morphology of the NBCCF@GDC oxygen electrode is shown in the inserted of Fig. 3(a). The NBCCF@GDC oxygen electrode is uniform with high porosity, which is beneficial to the adsorption and dissociation of oxygen. Fig. 3(b) shows the HRTEM results of the sample. The lattice spacing of 2.15 Å in position 1 is indexed as the (103) plane of the double perovskite structure, as confirmed by PDF #70-4074. Another lattice fringe spacing of 2.65 Å in position 3 is the (220) plane of the fluorite structure (PDF #75-0161). Position 2 has both overlapped phases which can be confirmed by FFT as shown in Fig. 3(b) insert. The morphology of the NBCCF@GDC composite powders is displayed in Fig. 3(c). It can be seen that the NBCCF@GDC composite powders agglomerate by many nanoparticles. However, it difficult to separate GDC and NBCCF in the composite, since both GDC and NBCCF grains are nanoscale and distribute homogeneously, which should provide more TPB for the electrode reaction. In addition, the homogeneous distribution for Nd, Ba, Ca, Co, Fe, Gd, Ce and O elements further confirms that NBCCF and GDC are uniformly distributed in the composite, as shown in Fig. 3(c). There is no aggregation of cations in the two phases during the preparation using one-pot method. In addition, the chemical composition of the synthesized composite is close to the theoretical stoichiometric ratio (Fig. S1, see supporting information).
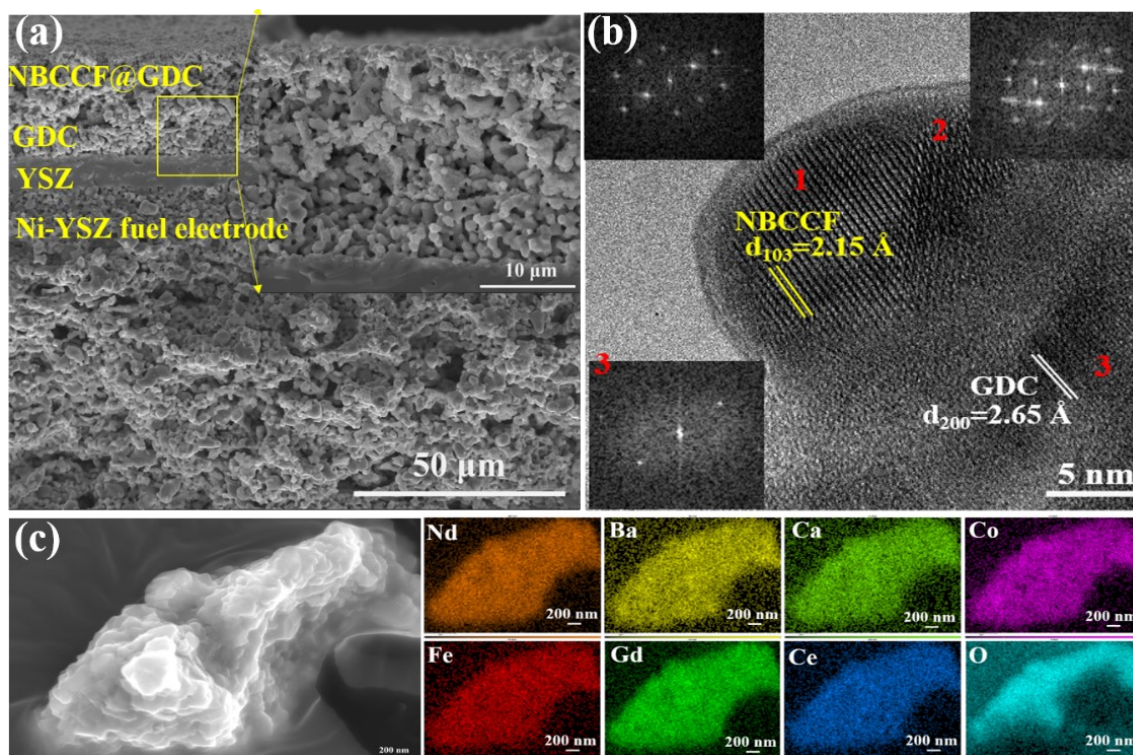
Fig. 3 The cross-sectional microstructure for fuel cell with the NBCCF@GDC oxygen electrode (a); The phase composition of NBCCF@GDC composite powders with FFT(b); The morphology of the NBCCF@GDC composite powders corresponding EDS mapping (c).

3.3. Electrochemical performance in SOFC mode

In this section we discuss a thorough characterization of the electrochemical performance of the electrodes when incorporated in full cells. First is a discussion of the electrochemical performance in fuel cell and electrolysis modes, followed by the reversibility and stability of the cells under continued operation. An important factor in the stability and performance of oxygen electrodes is their polarization resistance (Rp). Low Rp is desired since it means better ORR and OER performance. Fig. 4 summaries the Rp of the two electrodes and their electrochemical performance when incorporated in a full cell. From Fig. 4(a) and Fig. S2 it can be seen that NBCCF@GDC presents significantly lower Rp than NBCCF-GDC at all of the tested temperatures.

This enhancement can also be demonstrated through full cell performance measurements. In

SOFC mode, the open circuit voltages of both cells are high (Fig. 4(b) and Fig. S3(a)), indicating that the YSZ electrolyte is fully densified and the cell is well sealed. The peak power density (~ 1.3 W cm^{-2}) of the NBCCF@GDC cell is 40 % higher than that of the cell with the NBCCF-GDC oxygen electrode (~ 0.94 W cm^{-2}) at 800 °C. The electrochemical performance of the cells with NBCCF@GDC oxygen electrode in SOFC mode at different temperatures is displayed in Fig. S3. Nyquist plots of two cells at 800 °C are presented in Fig. 4(c). The Rp is generally represented by the range between the intersections of the high and low frequencies in the Nyquist plots. At the benchmark of 800 °C, NBCCF@GDC shows a Rp of 0.10 Ω cm^2 compared to 0.14 Ω cm^2 for NBCCF-GDC, showing a similar trend to that observed in Fig. 4(a). Importantly, both of these values are lower than comparable systems, as summarized in Table S1. The DRT spectra with four peaks are identified in the frequency range as shown in Fig. 4(d). Each peak corresponds to an electrode process, including the ion transport and the electron transfer (P1), the gas diffusion (P3) of the hydrogen electrode, the oxygen surface exchange (P2) and the gas diffusion (P4) of the oxygen electrode from high frequency to low frequency [37]. The P2 peak of NBCCF@GDC cell is significantly lower than that of NBCCF-GDC, indicating that it has good surface oxygen exchange performance and ORR activity.

3.4. Electrochemical performance in SOEC mode

The OER performance of the cell with NBCCF@GDC in SOEC mode is characterized by electrolysis of H$_2$O. Fig. 4(e) presents the I-V curves of two cells at 800 °C with 70 vol% AH. The current density of NBCCF@GDC cell is about 1.45 A cm^{-2} at 1.3 V, about 30% higher than that of NBCCF-GDC cell (1.11 A cm^{-2}) at 800 °C. The EIS of two cells under SOEC mode at 800 °C are presented in Fig. 4(f). Polarization resistance of the cell with NBCCF@GDC is significantly smaller than that of the cell with NBCCF-GDC (0.068 $\Omega \cdot$cm^2 vs 0.087 $\Omega \cdot$cm^2) at 800 °C. And it is also lower than the other reported results in Table S1. The I-V curves and EIS of the NBCCF@GDC

cell in SOEC mode at various humidities and temperatures are presented in Fig. S3. Moreover, the hydrogen production rate of NBCCF@GDC cell is up to 1744.73 mL $cm^{-2} \cdot h^{-1}$ at 2.0 V at 850 °C with 70 %AH (Fig. S4). It is worth noticing that there exists a smooth transition around OCV in the IV curve, suggesting favorable reversibility of SOCs with NBCCF@GDC.
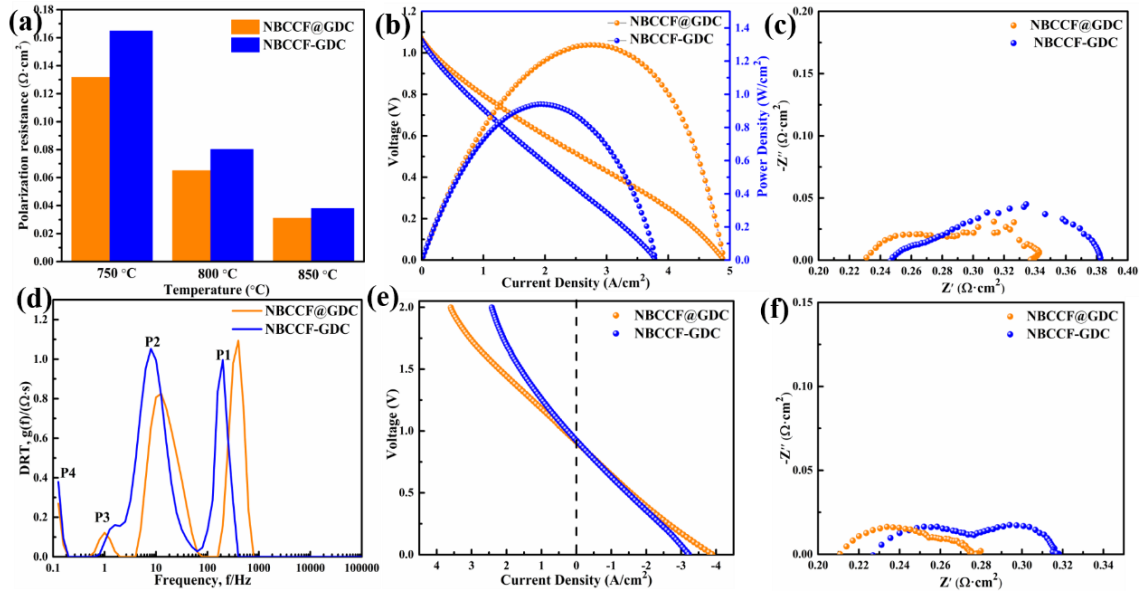

Fig. 4 The polarization resistance (Rp) of two electrodes in air at different temperature (a); the current density-voltage-power density curves (b); Nyquist plots (c) and DRT spectra (d) of two cells under SOFC mode at 800 °C; the current density-voltage curves (e); Nyquist plots (f) of two cells for H_2O electrolysis at 800 °C with 70 %AH.

3.5. Reliability of SSOCs

To investigate the electrochemical performance of SOCs in both fuel- and electrolysis cell modes at operating conditions, Nyquist plots of SOCs in polarization current density were measured. Fig. 5(a) shows the EIS of SOCs with different oxygen electrode in SOFC mode (-0.4 A cm^{-2}). The value of Rp of NBCCF@GDC cell is only 0.084 $\Omega \cdot cm^2$ at 800 °C, which is relatively lower than that of NBCCF-GDC cell (0.097 $\Omega \cdot cm^2$). This is because the oxygen surface exchange of NBCCF@GDC is better than NBCCF-GDC, as shown in Fig. S5(b). In SOEC mode, Rp of NBCCF@GDC cell (0.098 $\Omega \cdot cm^2$) is also lower than NBCCF-GDC cell (0.146 $\Omega \cdot cm^2$) at 800 °C

as shown in Fig. 5(b), indicating that NBCCF@GDC has the higher OER performance. It can be further demonstrated by DRT results in Fig. S5(d). The EIS of NBCCF@GDC cell operated in various conditions of 0.2, 0.4 and 0.6 A cm^{-2} in electrolysis cell mode are shown in Fig. 5(c). Except for the current density, no noticeable resistance fluctuation can be found, which proves the remarkable stability of the cell. Besides, the NBCCF@GDC cell shows a significant enhanced H_2O-CO_2 co-electrolysis performance compared to the NBCCF-GDC cell as shown in Fig. 5(d), with current density increasing from 0.58 to 1.19 A cm^{-2} at 1.4 V. The corresponding EIS of two cells are measured under OCV and operating conditions (1.4 V), as shown in Fig. 5(e, f). Polarization resistance decreases from 0.213 to 0.169 $\Omega \cdot cm^2$ at OCV or 0.366 to 0.195 $\Omega \cdot cm^2$ at 1.4 V. The detail co-electrolysis performance of NBCCF@GDC cell with different feed gas compositions is also investigated as shown in Fig. S6.
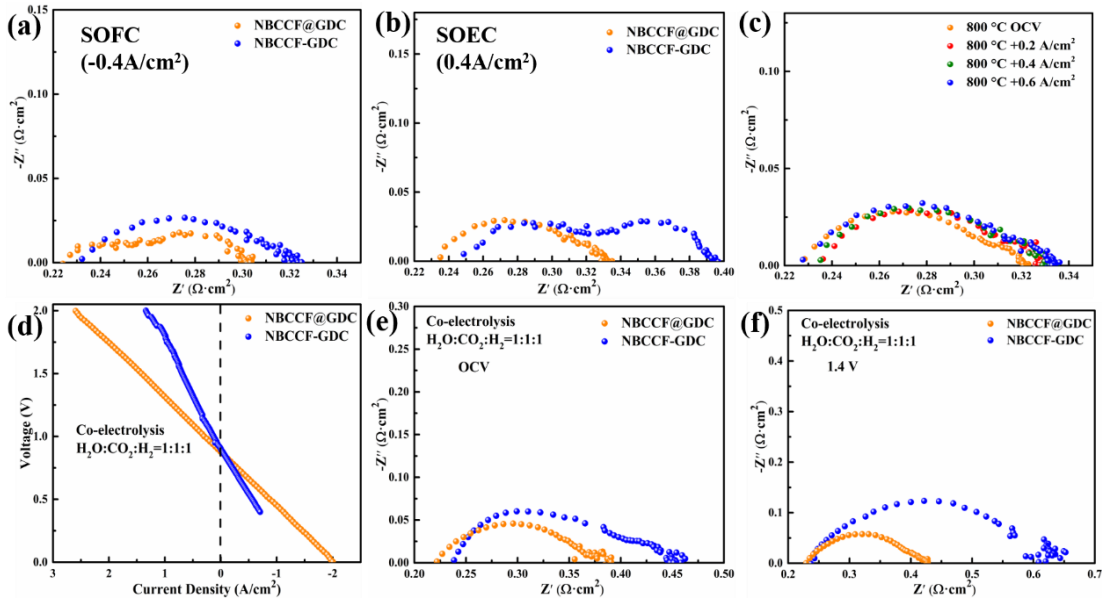

Fig. 5 EIS of two cells in working condition SOFC mode (a) and SOEC mode (b) at 800 °C; EIS of NBCCF@GDC cell at different current densities in SOEC mode (c); I-V curves of two cells for H_2O-CO_2 co-electrolysis (d); EIS of NBCCF@GDC cell at OCV (e) and 1.4 V (f) for H_2O-CO_2 co-electrolysis at 800 °C.

The consistently low Rp and high current densities observed in these NBCCF@GDC cells therefore demonstrate excellent OER performance of this oxygen electrode, favorably comparable with other composite perovskite oxide systems. However, another key metric is the reversibility and stability of the electrodes under continued operation. To investigate this, Nyquist plots of NBCCF@GDC cell in SOFC and SOEC modes were measured, as shown in Fig. 6(a). Rp is 0.068 $\Omega \cdot cm^2$, 0.098 $\Omega \cdot cm^2$ and 0.088 $\Omega \cdot cm^2$ under OCV, SOEC (0.4 A cm^{-2}) and SOFC modes (-0.4 A cm^{-2}), respectively. Rp in SOEC mode is slightly inferior to that in SOFC mode, which is consistent with results reported in previous literature [38, 39]. From Fig. 6(b), the lower peak intensity of P2 and P4 in SOFC mode compared with SOEC mode indicates better performance in SOFC mode. Overall, the NBCCF@GDC cell shows near-perfect reversibility, which coincides with the extremely smooth transition between SOFC and SOEC mode of the I-V curve. In addition, it exhibits good reversibility and stability with the short time interval as shown in Fig. S7(a). During the long-term intervals, the cell also shows no obvious attenuation during the reversible operation for up to 120 h as shown in Fig. 6(d). Even if the cell is continuously operated for 24 h in SOFC and SOEC mode, it still performs stably without obvious performance degradation (Fig. 6(c)). Moreover, the NBCCF@GDC cell also shows good stability for H_2O-CO_2 co-electrolysis (Fig. S7(b)). In addition to the performance stability, the microstructure of NBCCF@GDC cell is also relatively stable: no delamination or elemental diffusion was observed after the test (Fig. S8) and the crystal structure of the NBCCF@GDC oxygen electrode after test remains stable (Fig. S9).
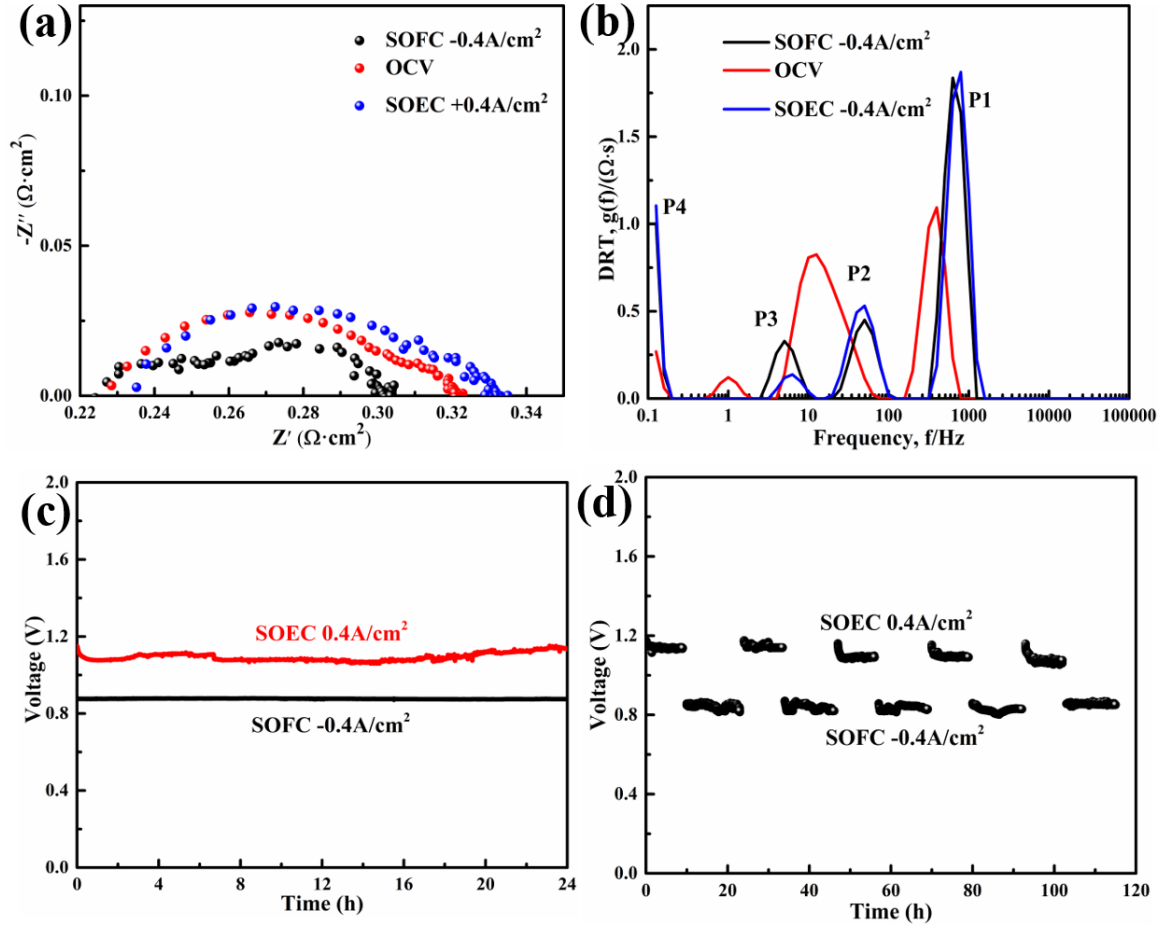
Fig. 6 EIS (a) and DRT curves(b) of the NBCCF@GDC cell measured at 800 °C with 70 vol%

AH under OCV, SOFC and SOEC mode; 24 h test in independent SOFC or SOEC mode (c) and

120 h reversible operation at 800 ºC (d).

4. The enhancement mechanism

Considering the excellent electrochemical performance and stability of NBCCF@GDC, we

investigate the origin of the improved performance induced by this novel one-pot method in detail.

The potential coherency between NBCCF and GDC phases in the NBCCF@GDC composite at

elevated temperature was examined by high-temperature XRD analysis as shown in Fig. 7(a, b).

There exist separate two phases at room temperature (NBCCF, GDC). However, the two separated

peaks at around 15º merge together as the temperature increases, indicating a phase contiguity and

interfacial coherence between NBCCF and GDC at working temperature [40, 41]. In addition, when

15

the temperature decreases back to room temperature (Fig. S10), the peak is again divided into two peaks representing two phases. However, there is no such phenomenon in NBCCF-GDC (Fig. S11). Moreover, the unit cell parameters of GDC and NBCCF in NBCCF@GDC are larger than those of NBCCF-GDC under corresponding conditions (Fig. S12), which indicates a strong interaction between NBCCF and GDC in NBCCF@GDC. Additional evidence of this can be seen from the HAADF-STEM results in Fig. 7(c). GDC has a well-ordered crystalline structure with the lattice spacing of 0.304 nm assigned to (111) plane, while a well-defined lattice spacing 0.769 nm is from the (001) plane of the double perovskite-type NBCCF. It is worth noting that there exist the grain boundary planes of NBCCF and GDC, which are relatively tight (as shown by the arrow). Moreover, fine particles are tightly assembled together which result in a high specific surface area and good electrocatalytic activity site (Fig. S13(a)) which likely facilitates charge transfer (e^- and O^{2-}) between the two components. In addition, the corresponding SAED patterns also demonstrates the co-existence of the two phases (Fig. S13(b)). EDS elemental mappings of Nd, Ba, Ca, Co, Fe, Ce, O are obviously overlapped, which suggests the formation of homogeneous and well-knit NBCCF@GDC. However, for NBCCF-GDC, Ce is shown to be absent by EDS mapping, suggesting that directly mixing NBCCF and GDC does not form a so coherently (Fig. S14).
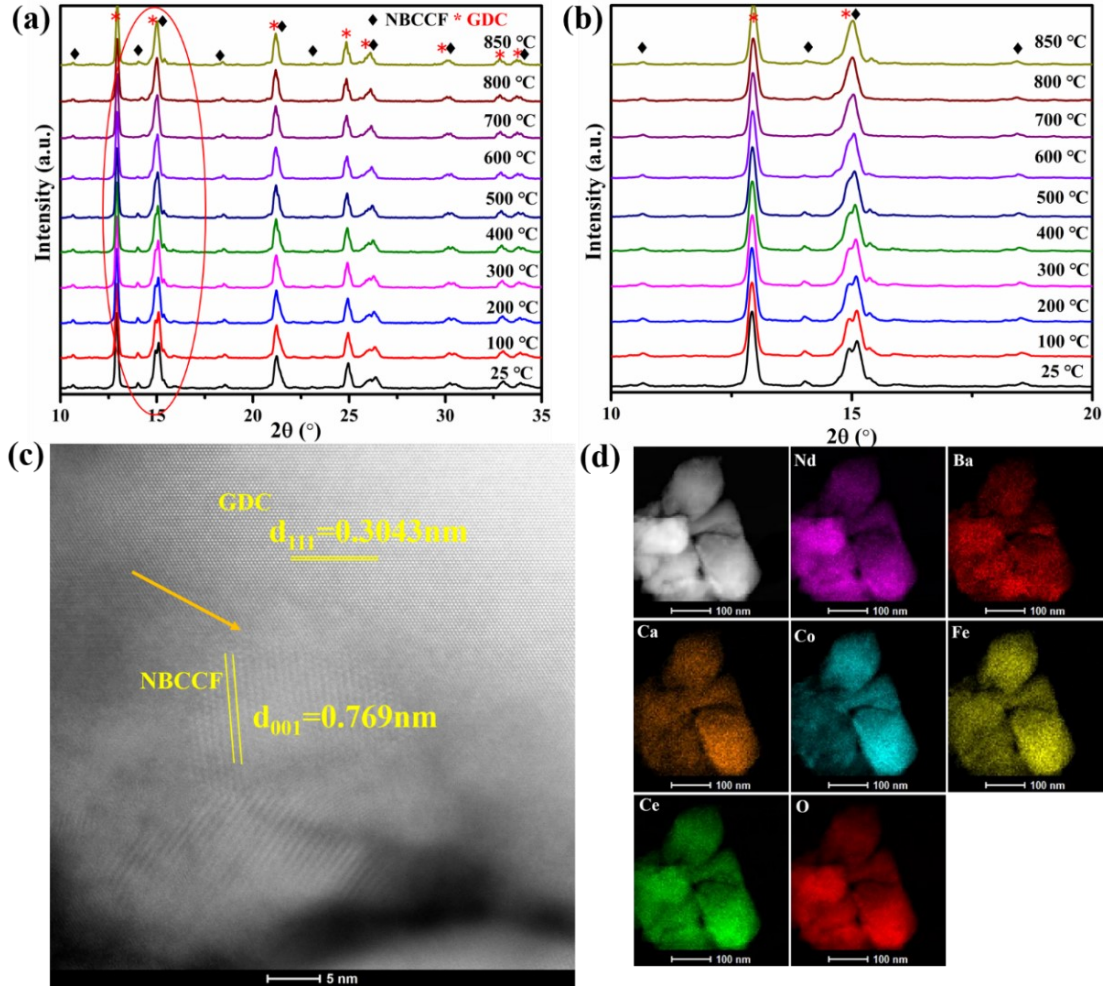
Fig. 7 High-temperature XRD patterns for NBCCF@GDC (a, b); HAADF-STEM of NBCCF@GDC (c) and the corresponding elemental mapping of NBCCF@GDC (d).

To further investigate the interface properties of NBCCF@GDC and NBCCF-GDC, EELS is examined which is in theory capable of measuring atomic composition, chemical bonding, valence and conduction band electronic properties, surface properties and element-specific pair distance distribution functions [21, 42, 43]. There is no Ce signal for NBCCF-GDC indicating that the NBCCF dimensions scale (Fig. 8(a)). The fine structure of Co $L_{2,3}$- edge is very effectual to determine the Co oxidation state on account and GDC phases are discretely separated at their particle of the transition from 2p3/2 and 2p1/2 electrons to 3d orbitals [8]. Despite the overlapping between Ba $M_{4,5}$-edges and Co $L_{2,3}$-edges, compared to NBCCF-GDC (Fig. 8(b)), an obvious peak change can

still be observed for NBBCF@GDC, which indicates the change of Co valence state. The energy difference (ΔEL_2–L_3= EL_2–EL_3) of NBCCF-GDC is 15.4 eV while 15.3 eV can be achieved for NBCCF@GDC. The small decrease of this value, in addition to the slight increase in energy (chemical shift) of the Co $L_{2,3}$ edges compared to NBCCF-GDC, suggests an increased valence of Co in NBCCF@GDC [44, 45], consistent with the results of FTIR in Fig. S15 and XPS in Fig 8(d), thus providing further evidence of the existence of coherence effect.

In order to obtain more insight into the coherence effect, we further analyzed the O K-edges of two samples. The coordination subtly influences the O K-edge fine structure, thus information about electronic excitations from O 1s to O 2p band can be provided for NBCCF@GDC. The feature of O K-edges is attributed to four main peaks. Specifically, peak A results from hybridization with Co 3d and Fe 3d, while peak B is hybridized with Nd 5d, Ca 3d and Ba 3d, and peaks C and D are thought to be contributed by Co 4sp and Fe 4sp as well as scattering resonance of adjacent atoms [46]. With increasing Co valence state, higher intensity peak A forms together with the increasing energy difference between peak A and peak B, as shown in Fig. 8(c). All these findings indicate an increase of Co valence in NBCCF@GDC, which can be further confirmed by XPS in Fig. 8(d, e). The Co 3p profile reveals an increasing Co valence of NBCCF@GDC (Co^{4+}/Co^{3+}=3.76) compared with NBCCF-GDC (Co^{4+}/Co^{3+}=2.84). Furthermore, the increasing Oad/Olat ratio indicates that the oxygen activity of NBCCF@GDC is enhanced with more oxygen-containing adsorbates that are beneficial to electrocatalytic activity [47, 48].

These results show that the NBCCF and GDC phases are discretely separated at their particle dimensions scale by the traditional physical mixing method. However, when NBCCF and GDC are synthesized by the one pot method, the NBCCF and GDC phases are tightly assembled together with homogeneous elemental distribution, resulting in high specific surface area (Fig. 2(d)) which likely facilitates charge transfer (e^- and O^{2-}) between the two components. In addition, the length

of TPB will increase and result in more reactivity sites. It is worth noting that the phase contiguity and interfacial coherence between NBCCF and GDC will increase the Co oxidation state and the amount of oxygen-containing adsorbates, resulting in the overlap between the occupied O 2p valence bands and the unoccupied TM 3d conduction bands [49, 50]. This lowers the Fermi level into the O 2p band which has been correlated with both increased conductivity (Fig. 2(e)) and electrocatalytic activity for perovskites (Fig. 8(f)) [51-53].

Fig. 8 (a) STEM-EELS profiles of NBCCF@GDC and NBCCF-GDC (a), and Co L2,3-edges (b) and O K-edges (c) of two samples; XPS Co3p profile (d) and O1s profile (e) of NBCCF@GDC and NBCCF-GDC; relationship between O2p band center and Co–O bond covalency (f).

5. Conclusion

In this work, $NdBa_{0.5}Ca_{0.5}Co_{1.5}Fe_{0.5}O_{5+\delta}@Gd_{0.1}Ce_{0.9}O_{2-\delta}$ composite has been synthesized by a novel one-pot method, and applied as a promising oxygen electrode for reversible solid oxide cells. Such a composite electrode prepared by this method has a high specific surface area and significantly improved ORR, OER performance than the traditional physical mixing route. The

maximum power density of 1.3 W cm^{-2} and polarization resistance of 0.106 Ω cm^2 at 800 °C can be achieved in fuel cell mode. While in electrolysis mode, the current density can reach 1.452 A cm^{-2} at 800 °C with 70 vol% AH at 1.3 V. Notably, strong coherency in these NBCCF@GDC composite materials was successfully revealed by HT-XRD, XPS, STEM and EELS. The phase contiguity and interfacial coherence between NBCCF and GDC increase the Co oxidation state and the number of active sites, which enhanced the electrocatalytic activity for perovskites. Overall, it provides a general strategy for the functionalization electrode of reversible solid oxide cells.

ASSOCIATED CONTENT

Supporting Information

The Supporting Information is available free of charge on the ACS Publications website at DOI:xxxx.

Additional information on the EIS of NBCCF@GDC and NBCCF-GDC half-cell at 700-850 °C, Electrochemical performance of NBCCF@GDC single cell in SOFC mode; I-V curves and EIS of NBCCF@GDC cell with different feed gas compositions at 800 °C. Cross-section view and EDS mapping of the cell after the test. The in-situ XRD of NBCCF@GDC powders in the cooling process; FT-IR spectra of the NBCCF-GDC and NBCCF@GDC samples (PDF).

AUTHOR INFORMATION

Corresponding Author

*Bo Chi - Center for Fuel Cell Innovation, School of Materials Science and Engineering, Huazhong University of Science and Technology, Wuhan 430074, China; Email: chibo@hust.edu.cn

Author contributions

Notes

The authors declare no competing financial interest.

REFERENCES

[1] Zaman, K.; Moemen, M.A.-e., Energy consumption, carbon dioxide emissions and economic development: Evaluating alternative and plausible environmental hypothesis for sustainable growth. *Renew.Sust. Energ. Rev.,* **2017,** *74*, 1119-1130.

[2] Lee, D.-G.; Kim, S.H.; Joo, S.H.; Ji, H.-I.; Tavassol, H.; Jeon, Y.; Choi, S.; Lee, C. Kim, M.-H.; Kwak, S.K.; Kim, G.; Song, H.-K., Polypyrrole-assisted oxygen electrocatalysis on perovskite oxides. *Energy Environ. Sci*, **2017,** 10, 523-527.

[3] Gao, S.; Lin, Y.; Jiao, X.; Sun, Y.; Luo, Q.; Zhang, W.; Li, D.; Yang, J.; Xie, Y., Partially oxidized atomic cobalt layers for carbon dioxide electroreduction to liquid fuel. *Nature*, **2016,** *529*, 68-71.

[4] Guo, Y.; Niu, P.; Liu, Y.; Ouyang, Y.; Li, D.; Zhai, T.; Li, H.; Cui, Y., An Autotransferable g-C_3N_4 Li(+) -Modulating Layer toward Stable Lithium Anodes. *Adv. Mater.*, **2019,** e1900342.

[5] Wu, C.; Wang, K.; Yan, Y.; Yang, D.; Jiang, Y.; Chi, B.; Liu, J.; Esker, A.R.; Rowe, J.; Morris, A.J.; Sanghadasa, M.; Priya, S., Fullerene Polymer Complex Inducing Dipole Electric Field for Stable Perovskite Solar Cells. *Adv. Funct. Mater.*, **2019,** *29*, 1804419.

[6] Zhang, S.-L.; Wang, H.; Lu, M.Y.; Zhang, A.-P.; Mogni, L.V.; Liu, Q.; Li, C.-X.; Li, C.-J.; Barnett, S.A., Cobalt-substituted $SrTi_{0.3}Fe_{0.7}O_{3-\delta}$: a stable high-performance oxygen electrode material for intermediate-temperature solid oxide electrochemical cells. *Energy Environ. Sci*, **2018,** *11*, 1870-1879.

[7] Jensen, S.H.; Graves, C.; Mogensen, M.; Wendel, C.; Braun, R.; Hughes, G.; Gao, Z.; Barnett, S.A., Large-scale electricity storage utilizing reversible solid oxide cells combined with underground storage of CO_2 and CH_4. *Energy Environ. Sci*, **2015,** *8*, 2471-2479.

[8] Li, M.; Hua, B.; Chen, J.; Zhong, Y.; Luo, J.-L., Charge transfer dynamics in RuO_2/perovskite nanohybrid for enhanced electrocatalysis in solid oxide electrolyzers. *Nano Energy*, **2019,** *57*, 186-194.

[9] Ai, N.; Li, N.; He, S.; Cheng, Y.; Saunders, M.; Chen, K.; Zhang, T.; Jiang, S.P., Highly active and stable $Er_{0.4}Bi_{1.6}O_3$ decorated $La_{0.76}Sr_{0.19}MnO_{3+\delta}$ nanostructured oxygen electrodes for reversible solid oxide cells. *J. Mater. Chem. A*, **2017,** *5*, 12149-12157.

[10] Tian, Y.; Li, J.; Liu, Y.; Yang, J.; Liu, B.; Jia, L.; Jiang, J.; Chi, B.; Pu, J.; Li, J., Preparation and properties of $PrBa_{0.5}Sr_{0.5}Co_{1.5}Fe_{0.5}O_{5+\delta}$ as novel oxygen electrode for reversible solid oxide electrochemical cell. *Int. J. Hydrog. Energy*, **2018,** *43*, 12603-12609.

[11] Jun, A.; Yoo, S.; Ju, Y.-W.; Hyodo, J.; Choi, S.; Jeong, H. Y.; Shin, J.; Ishihara, T.; Lim, T.-h.; Kim, G., Correlation between fast oxygen kinetics and enhanced performance in Fe doped layered perovskite cathodes for solid oxide fuel cells. *J. Mater. Chem. A*, **2015,** *3*, 15082-15090.

[12] Kim, J.; Seo, W.-y.; Shin, J.; Liu, M.; Kim, G.; Composite cathodes composed of $NdBa_{0.5}Sr_{0.5}Co_2O_{5+\delta}$ and $Ce_{0.9}Gd_{0.1}O_{1.95}$ for intermediate-temperature solid oxide fuel cells. *J. Mater. Chem. A*, **2013,** *1*, 515-519.

[13] Chen, Y.; Yoo, S.; Choi, Y.; Kim, J. H.; Ding, Y.; Pei, K.; Murphy, R.; Zhang, Y.; Zhao, B.; Zhang, W.; Chen, H.; Chen, Y.; Yuan, W.; Yang, C.; Liu, M., A highly active, CO_2-tolerant electrode for the oxygen reduction reaction. *Energy Environ. Sci*, **2018,** *11*, 2458-2466.

[14] Du, Z.; Yan, C.; Zhao, H.; Zhang, Y.; Yang, C.; Yi, S.; Lu, Y.; Świerczek, K., Effective Ca-doping in $Y_{1-x}Ca_xBaCo_2O_{5+\delta}$ cathode materials for intermediate temperature solid oxide fuel cells. *J. Mater. Chem. A*, **2017,** *5*, 25641-25651.

[15] Lim, C.; Jun, A.; Jo, H.; Ok, K. M.; Shin, J.; Ju, Y.-W.; Kim, G., Influence of Ca-doping in layered perovskite $PrBaCo_2O_{5+\delta}$ on the phase transition and cathodic performance of a solid oxide fuel cell. *J. Mater. Chem. A*, **2016,** *4*, 6479-6486.

[16] Choi, S.; Park, S.; Shin, J.; Kim, G., The effect of calcium doping on the improvement of performance and durability in a layered perovskite cathode for intermediate-temperature solid oxide fuel cells. *J. Mater. Chem. A*, **2015,** *3*, 6088-6095.

[17] Hua, B.; Zhang, Y.-Q.; Yan, N.; Li, M.; Sun, Y.-F.; Chen, J.; Li, J.; Luo, J.-L.; The Excellence of Both Worlds: Developing Effective Double Perovskite Oxide Catalyst of Oxygen Reduction Reaction for Room and Elevated Temperature Applications. *Adv. Funct. Mater.*, **2016,** *26*, 4106-4112.

[18] Choi, M.-B.; Singh, B.; Wachsman, E. D.; Song, S.-J., Performance of $La_{0.1}Sr_{0.9}Co_{0.8}Fe_{0.2}O_{3-\delta}$ and $La_{0.1}Sr_{0.9}Co_{0.8}Fe_{0.2}O_{3-\delta}$–$Ce_{0.9}Gd_{0.1}O_2$ oxygen electrodes with $Ce_{0.9}Gd_{0.1}O_2$ barrier layer in reversible solid oxide fuel cells. *J. Power Sources*, **2013,** *239*, 361-373.

[19] Liang, M.; Yu, B.; Wen, M.; Chen, J.; Xu, J.; Zhai, Y., Preparation of LSM–YSZ composite powder for anode of solid oxide electrolysis cell and its activation mechanism. *J. Power Sources*, **2009,** *190*, 341-345.

[20] Zhang, X.; Liu, L. ; Zhao, Z.; Tu, B.; Ou, D.; Cui, D.; Wei, X.; Chen, X.; Cheng, M., Enhanced oxygen reduction activity and solid oxide fuel cell performance with a nanoparticles-loaded cathode. *Nano Lett.*, **2015,** *15*, 1703-1709.

[21] Chen, Y.; Chen, Y.; Ding, D.; Ding, Y.; Choi, Y.; Zhang, L.; Yoo, S.; Chen, D.; Glee, B.; Xu, H.; Lu, Q.; Zhao, B.; Vardar, G.; Wang, J.; Bluhm, H.; Crumlin, E.J.; Yang, C.; Liu, J.; Yildiz, B.; Liu, M., A robust and active hybrid catalyst for facile oxygen reduction in solid oxide fuel cells. *Energy Environ. Sci*, **2017,** *10*, 964-971.

[22] Tsekouras, G.; Neagu, D.; Irvine, J.T.S., Step-change in high temperature steam electrolysis performance of perovskite oxide cathodes with exsolution of B-site dopants. *Energy Environ. Sci.*, **2013,** *6*, 256-266.

[23] Neagu, D.; Oh, T.S.; Miller, D.N.; Menard, H.; Bukhari, S.M.; Gamble, S.R.; Gorte, R.J.; Vohs, J.M.; Irvine, J.T.S., Nano-socketed nickel particles with enhanced coking resistance grown in situ by redox exsolution. *Nat. Commun.*, **2015,** *6*, 8120.

[24] Myung, J.H.; Neagu, D.; Miller, D.N.; Irvine, J.T., Switching on electrocatalytic activity in

solid oxide cells. *Nature,* **2016,** *537*, 528-531.

[25] Tan, Y. ; Wang, A.; Jia, L.; Yan, D.; Chi, B.; Pu, J.; Li, J., High-performance oxygen electrode for reversible solid oxide cells with power generation and hydrogen production at intermediate temperature. *Int. J. Hydrog. Energy*, **2017,** *42*, 4456-4464.

[26] Irvine, J.T.S.; Neagu, D.; Verbraeken, M.C.; Chatzichristodoulou, C.; Graves, C.; Mogensen, M.B., Evolution of the electrochemical interface in high-temperature fuel cells and electrolysers. *Nat. Energy*, **2016,** *1*, 15014.

[27] Hua, B.; Li, M.; Sun, Y.-F.; Li, J.-H.; Luo, J.-L., Enhancing Perovskite Electrocatalysis of Solid Oxide Cells Through Controlled Exsolution of Nanoparticles. *ChemSusChem*, **2017,** *10*, 3333-3341.

[28] Tian, Y.; Zheng, H.; Zhang, L.; Chi, B.; Pu, J.; Li, J., Direct Electrolysis of CO_2 in Symmetrical Solid Oxide Electrolysis Cell Based on $La_{0.6}Sr_{0.4}Fe_{0.8}Ni_{0.2}O_{3-\delta}$ Electrode. *J. Electrochem. Soc*, **2018,** *165*, F17-F23.

[29] Tan, Y.; Duan, N.; Wang, A.; Yan, D.; Chi, B.; Wang, N.; Pu J.; Li, J., Performance enhancement of solution impregnated nanostructured $La_{0.8}Sr_{0.2}Co_{0.8}Ni_{0.2}O_{3-\delta}$ oxygen electrode for intermediate temperature solid oxide electrolysis cells. *J. Power Sources*, **2016,** *305*, 168-174.

[30] Wang, A.; Pu, J.; Yan, D.; Duan, N.-Q.; Tan, Y.; Jia, L.; Chi, B.; Li, J., Promoted electrochemical performance of intermediate temperature solid oxide fuel cells with $Pd_{0.95}Mn_{0.05}O$-infiltrated $(La_{0.8}Sr_{0.2})_{0.95}MnO_{3-\delta}–Y_{0.16}Zr_{0.84}O_2$ composite cathodes. *J. Power Sources*, **2016,** *303*,137-141.

[31] Sonn, V.; Leonide A.; Ivers-Tiffée, E., Combined deconvolution and CNLS fitting approach applied on the impedance response of technical Ni / 8YSZ cermet electrodes. *J. Electrochem. So*c, **2008,** *155*, B675.

[32] Liu, B.; Muroyama, H.; Matsui, T.; Tomida, K.; Kabata T.; Eguchi, K., Analysis of impedance

spectra for segmented-in-series tubular solid oxide fuel cells. *J. Electrochem. Soc*. **2010,** *157*, B1858.

[33] Zhao, C.; Li, Y.; Zhang, W.; Zheng, Y.; Lou, X.; Yu, B.; Chen, J.; Chen, Y.; Liu, M.; Wang, J., Heterointerface engineering for enhancing the electrochemical performance of solid oxide cells. *Energy Environ. Sci.*, **2020,** *13*, 53-85.

[34] Hayashi, H.; Kanoh, M.; Quan, C.J.; Inaba, H.; Wang, S.; Dokiya, M.; Tagawa, H., Thermal expansion of Gd-doped ceria and reduced ceria. *Solid State Ionics,* **2000,** *132*, 227-233.

[35] Ullmann, H.; Trofimenko, N.; Tietz, F.; Stöver, D.; Ahmad-Khanlou, A., Correlation between thermal expansion and oxide ion transport in mixed conducting perovskite-type oxides for SOFC cathodes. *Solid state ionics*, **2000,** *138*, 79-90

[36] Chen, G.; Sunarso, J.; Wang, Y.; Ge, C.; Yang, J.; Liang, F., Evaluation of A-site deficient $Sr_{1-x}Sc_{0.175}Nb_{0.025}Co_{0.8}O_{3-\delta}$ (x=0, 0.02, 0.05 and 0.1) perovskite cathodes for intermediate-temperature solid oxide fuel cells. *Ceram.Int.*, **2016,** *42*, 12894-12900.

[37] Yan, J.; Chen, H.; Dogdibegovic, E.; Stevenson, J.W.; Cheng, M.; Zhou, X.-D.; High-efficiency intermediate temperature solid oxide electrolyzer cells for the conversion of carbon dioxide to fuels. *J. Power Sources*, **2014,** *252*, 79-84.

[38] Tian, Y.; Wang, W.; Liu, Y.; Zhang, L.; Jia, L.; Yang, J.; Chi, B.; Pu, J.; Li, J., Cobalt-Free Perovskite Oxide $La_{0.6}Sr_{0.4}Fe_{0.8}Ni_{0.2}O_{3-\delta}$ as Active and Robust Oxygen Electrode for Reversible Solid Oxide Cells. *ACS Appl. Energy Mater.*, **2019,** *2*, 3297.

[39] Laguna-Bercero, M.A.; Kinadjan, N.; Sayers, R.; El Shinawi, H.; Greaves, C.; Skinner, S.J., Performance of $La_{2-x}Sr_xCo_{0.5}Ni_{0.5}O_{4\pm\delta}$ as an Oxygen Electrode for Solid Oxide Reversible Cells. *Fuel Cells*, **2011,** *11*, 102-107.

[40] Song, H. S.; Hyun, S. H.; Kim, J.; Lee, H.-W.; Moon, J., A nanocomposite material for highly durable solid oxide fuel cell cathodes. *Journal of Materials Chemistry*, **2008,** *18*, 1087-1092.

[41] Kumar, A.; Leonard, D.; Jesse, S.; Ciucci, F.; Eliseev, E. A.; Morozovska, A. N.; Biegalski, M. D.; Christen, H. M.; Tselev, A.; Mutoro, E., Spatially resolved mapping of oxygen reduction/evolution reaction on solid-oxide fuel cell cathodes with sub-10 nm resolution. *ACS Nano*, **2013,** *7*, 3808-3814.

[42] Klie, R.F.; Zhao, Y.; Yang, G.; Zhu, Y., High-resolution Z-contrast imaging and EELS study of functional oxide materials. *Micron*, **2008,** *39*, 723-733.

[43] Wang, Z.; Yin, J.; Jiang, Y., EELS analysis of cation valence states and oxygen vacancies in magnetic oxides. *Micron*, **2000,** *31*, 571-580.

[44] Carroll, K.J.; Qian, D.; Fell, C.; Calvin, S.; Veith, G.M.; Chi, M.; Baggetto, L.; Meng, Y.S., Probing the electrode/electrolyte interface in the lithium excess layered oxide $Li_{1.2}Ni_{0.2}Mn_{0.6}O_2$. *Phys. Chem. Chem. Phys.*, **2013,** *15*, 11128-11138.

[45] Wang, C.; Wang, Y.; Liu, X.; Yang, H.; Sun, J.; Yuan, L.; Zhou, G.; Rosei, F.; Structure versus properties inα-Fe_2O_3 nanowires and nanoblades. *Nanotechnology*,   **2016,** *27*, 035702.

[46] Sharifi-Asl, S.; Soto, F.A.; Nie, A.; Yuan, Y.; Asayesh-Ardakani, H.; Foroozan, T.; Yurkiv, V.; Song, B.; Mashayek, F.; Klie, R.F., Facet-dependent thermal instability in $LiCoO_2$. *Nano Lett.*, **2017,** *17*, 2165-2171.

[47] Lv, H.; Zhou, Y.; Zhang, X.; Song, Y.; Liu, Q.; Wang, G.; Bao, X., Infiltration of $Ce_{0.8}Gd_{0.2}O_{1.9}$ nanoparticles on $Sr_2Fe_{1.5}Mo_{0.5}O_6$- cathode for CO_2 electroreduction in solid oxide electrolysis cell. *J. Energy Chem*, **2019,** *35*, 71-78.

[48] Zhao, B.; Zhang, L.; Zhen, D.; Yoo, S.; Ding, Y.; Chen, D.; Chen, Y.; Zhang, Q.; Doyle, B.; Xiong, X.; Liu, M., A tailored double perovskite nanofiber catalyst enables ultrafast oxygen evolution. *Nat. Commun.*, **2017,** *8*, 14586.

[49] Grimaud, A.; May, K.J.; Carlton, C.E.; Lee, Y.L.; Risch, M.; Hong, W.T.; Zhou, J.; Shao-Horn, Y., Double perovskites as a family of highly active catalysts for oxygen evolution in alkaline
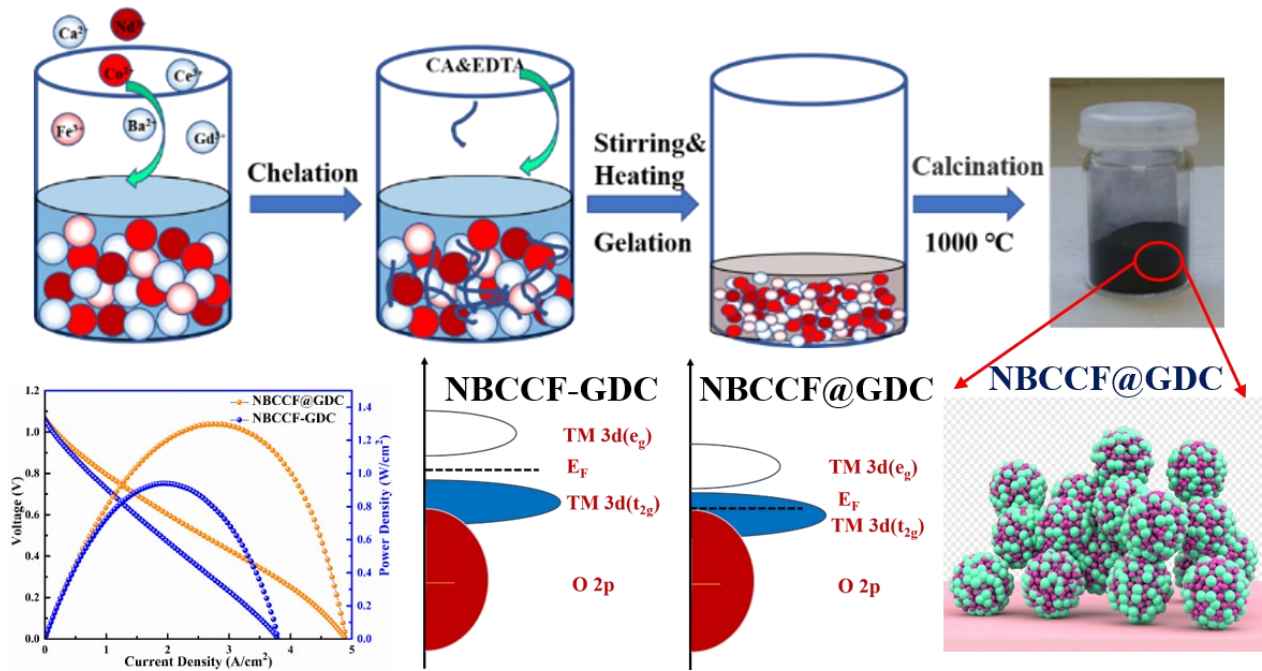
solution. *Nat. Commun.*, **2013,** *4*, 2439.

[50] Mueller, D.N.; Machala, M.L.; Bluhm, H.; Chueh, W.C., Redox activity of surface oxygen anions in oxygen-deficient perovskite oxides during electrochemical reactions. *Nat. Commun.*, **2015,** *6*, 6097.

[51] Mefford, J.T.; Rong, X.; Abakumov, A.M.; Hardin, W.G.; Dai, S.; Kolpak, A.M.; Johnston, K.P.; Stevenson, K.J., Water electrolysis on $La_{1-x}Sr_xCoO_{3-\delta}$ perovskite electrocatalysts. *Nat. Commun.*, **2016,** *7*, 11053.

[52] Hong, W.T.; Stoerzinger, K.A.; Lee, Y.-L.; Giordano, L.; Grimaud, A.; Johnson, J. Hwang, A.M.; Crumlin, E.J.; Yang, W.; Shao-Horn, Y., Charge-transfer-energy-dependent oxygen evolution reaction mechanisms for perovskite oxides. *Energy Environ. Sci.*, **2017,** *10*, 2190-2200.

[53] Hwang, J.; Rao, R.R.; Giordano, L.; Katayama, Y.; Yu, Y.; Shao-Horn, Y., Perovskites in catalysis and electrocatalysis. *Science*, **2017,** *358*, 751-756.

Table of Contents

Achieving Strong Coherency for Composite Electrode via One Pot Method with Enhanced Electrochemical Performance in Reversible Solid Oxide Cells